

Impacts of Mesoscale Wind on Turbulent Flow and Ventilation in a Densely Built-up Urban Area

SEUNG-BU PARK AND JONG-JIN BAIK

School of Earth and Environmental Sciences, Seoul National University, Seoul, South Korea

SANG-HYUN LEE

Department of Atmospheric Science, Kongju National University, Gongju, South Korea

(Manuscript received 29 January 2014, in final form 5 November 2014)

ABSTRACT

Turbulent flow in a densely built-up area of Seoul, South Korea, for 0900–1500 LST 31 May 2008 is simulated using the parallelized large-eddy simulation model (PALM) coupled to a mesoscale model (Weather Research and Forecasting Model). Time-varying inflow that is composed of mesoscale wind and turbulent signals induces different mean flows and turbulence structures depending on time. Sweeps induced by upper flow are distinct for 0900–0910 LST, and strong ejections and weaker sweeps are dominant for 1450–1500 LST at height $z = 200$ m. To investigate pedestrian wind environment and ventilation, mean wind velocity and turbulent kinetic energy at 2.5 m above streets are analyzed. The reference mean wind speed at $z = 600$ m continuously increases after 1010 LST. The pedestrian mean streamwise velocity tends to decrease after 1100 LST, although the pedestrian mean wind speed tends to slowly increase. Whereas the temporal velocity variations related to mesoscale wind are distinct in a street canyon and an intersection, the variations induced by mesoscale wind disappear in a dense building area, indicating strong decoupling from mesoscale wind. The velocity ratio of the pedestrian mean wind speed to the reference mean wind speed, representing a measure of ventilation in urban areas, is high on broad streets and at intersections and is low in dense building areas. Vortices in street canyons and winding flows around tall buildings seem to induce high velocity ratio there. The velocity ratio is shown to be linearly proportional to the pedestrian mean streamwise velocity.

1. Introduction

As urbanization continues, topics such as wind environment and air quality in densely built-up urban areas have attracted more interest. Complex urban morphology makes building-scale wind environment in urban areas highly complex, however, adding difficulties in predicting building- to city-scale urban air quality. Another important factor that complicates wind environment in urban areas is time-varying mesoscale meteorological conditions. Building-scale wind environment is shown to be sensitive to parameters such as background wind direction (Balogun et al. 2010) and atmospheric stability (Zhang et al. 1996; Santos et al. 2009), which are closely related to mesoscale meteorological conditions.

The impacts of urban morphology on wind environment have been extensively studied through laboratory experiments, field observations, and numerical simulations (Baik and Kim 1999; Cheng and Castro 2002; Kim and Baik 2004; Eliasson et al. 2006; Li et al. 2006; Coeal et al. 2006; Inagaki and Kanda 2010; Princevac et al. 2010). An increasing number of studies have recently been conducted to directly investigate wind environment over actual urban morphology with the help of digital elevation models (Nakayama et al. 2011, 2012; Letzel et al. 2012; Kanda et al. 2013).

Along with the use of actual urban morphology, the implementation of actual or simulated mesoscale meteorological conditions in computational fluid dynamics (CFD) models has been done (Ehrhard et al. 2000; Cox et al. 2000). One method to incorporate mesoscale meteorological conditions is to use high-tower measurement data as the lateral boundary conditions of CFD models (Xie 2011), but measurement data have limitations in their spatial coverage. To minimize the spatial

Corresponding author address: Jong-Jin Baik, School of Earth and Environmental Sciences, Seoul National University, Seoul 151-742, South Korea.
E-mail: jjbaik@snu.ac.kr

coverage problem, mesoscale-model data are employed as lateral or inflow boundary conditions for building-resolving CFD models. Ehrhard et al. (2000) investigated microscale wind environment in an industrial area in Germany with a model that was based on the Reynolds-averaged Navier-Stokes (RANS) equations, with mesoscale-model data being used as lateral boundary conditions. Baik et al. (2009) simulated flow and dispersion in an urban area in South Korea using a RANS model coupled to a mesoscale model (the fifth-generation Pennsylvania State University–National Center for Atmospheric Research Mesoscale Model) and investigated characteristic flow patterns around urban obstacles. Time-varying mesoscale-model data combined with/without artificially generated turbulent signals are used in large-eddy simulation (LES) models that resolve turbulent eddies around urban obstacles and require more computing times than RANS models (Nakayama et al. 2012; Liu et al. 2012; Wyszogrodzki et al. 2012). The feasibility of using a CFD model coupled to a mesoscale model to simulate urban flow and dispersion has been confirmed in the above studies. The impacts of mesoscale meteorological conditions are not yet sufficiently understood, however. It is important to clarify the possible impacts of mesoscale meteorological conditions on building-scale flow in urban areas.

In this study, we investigate the impacts of mesoscale wind on turbulent flow and ventilation in a densely built-up urban area using an LES model that is one-way coupled to a mesoscale model. In section 2, the LES model and mesoscale model are described. The simulation is validated with observations in section 3. The numerical results are presented and discussed in section 4. A summary and conclusions are provided in section 5.

2. Model description and simulation setup

To simulate turbulent flow in a densely built-up area of Seoul, South Korea, for 0900–1500 LST 31 May 2008, the parallelized LES model (PALM) developed at the Leibniz Universität Hannover (Raasch and Schröter 2001; Letzel et al. 2008) is used, with wind data from the Advanced Research version of the Weather Research and Forecasting (WRF) Model (Skamarock et al. 2008) being used as turbulent inflow boundary condition data for PALM. In this simulation, the WRF Model, version 3.2, with the Seoul National University Urban Canopy Model (SNUUCM; Ryu et al. 2011) is used. Five two-way nested computational domains are considered (Fig. 1a), and the horizontal grid sizes are 27, 9, 3, 1, and 0.333 km. The innermost domain covers the Seoul metropolitan area and includes the main domain of the LES model (Fig. 1b). There are 43 vertical layers below the

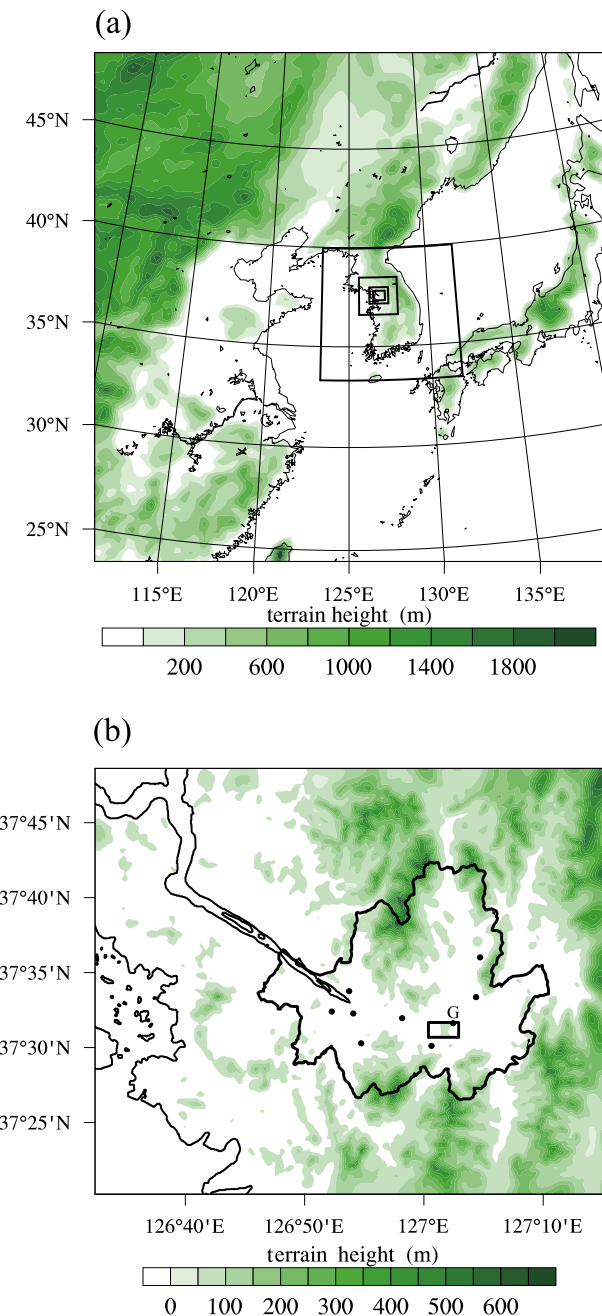


FIG. 1. Illustrations of (a) five domains and (b) innermost domain in the WRF-SNUUCM simulation with terrain elevation (shaded). The main domain is indicated by the inner rectangle with solid lines in (b). The nine automatic weather stations are indicated by filled circles in (b), and Gangnam automatic weather station is indicated with a G.

model top (20 hPa), and 16 vertical layers exist below 2 km to better resolve the lower atmosphere (close to the surface). A clear day with a slight variation of wind direction is considered in this study, and 31 May 2008, when a high pressure system was located around the

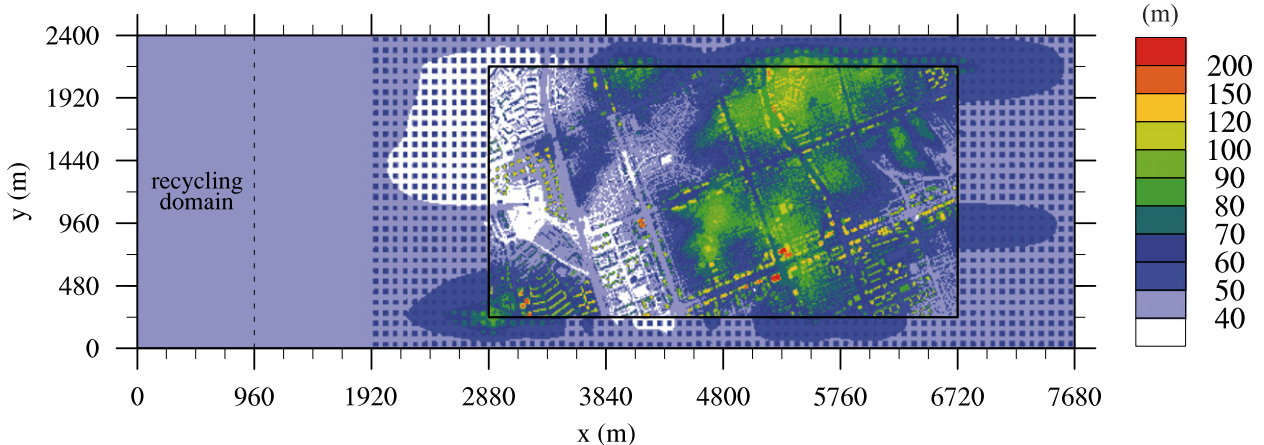


FIG. 2. Illustration of elevation field of ground and building-top surfaces in the LES model. The main domain is indicated by the inner rectangle with solid lines. (Adapted from Park et al. 2015.)

Korean Peninsula, is selected as the case day. The WRF Model is integrated for 48 h, starting from 0000 UTC 30 May 2008. The National Centers for Environmental Prediction final analysis data with $1^\circ \times 1^\circ$ horizontal resolution and 6-h intervals are used as initial and boundary conditions in the WRF simulation. The WRF single-moment six-class microphysics scheme (Hong and Lim 2006) is used to represent explicit cloud processes, and the updated Kain–Fritsch convective scheme (Kain 2004) is applied as a cumulus parameterization scheme for the first and second outermost domains. Radiative processes are represented with the Dudhia shortwave radiation scheme (Dudhia 1989) and the Rapid Radiative Transfer Model longwave radiation scheme (Mlawer et al. 1997). The planetary boundary layer processes are represented by the Yonsei University planetary boundary layer scheme (Hong et al. 2006), and the Noah land surface model (Chen and Dudhia 2001) is used.

PALM, which is based on the implicitly filtered Boussinesq equations, numerically solves the prognostic equations of momentum and subgrid-scale (SGS) turbulent kinetic energy (TKE) using the third-order Runge–Kutta scheme for time integration and the second-order Piacsek and Williams (1970) scheme for advection. The SGS turbulent momentum fluxes are parameterized using the 1.5-order Deardorff (1980) scheme.

A densely built-up area of Seoul ($3840\text{ m} \times 1920\text{ m}$ —the inner rectangular region in Figs. 1b and 2) is selected in this study (Park et al. 2015). The selected area (main domain) includes high-rise buildings, broad streets, and apartment complexes (Fig. 2). The average building height is $\sim 15\text{ m}$, and the height of the tallest building is 206 m . The ground elevation varies from ~ 30 to $\sim 90\text{ m}$, and this variation makes the calculation of canopy

height difficult. Airborne light detection and ranging (lidar) data are converted to 5-m gridded elevation data, and the converted data are used as the bottom boundary of the LES model. Buffer regions are added around the lateral boundaries of the selected area. In the buffer regions, the variation of ground elevation at the lateral boundaries of the selected area is smoothed out toward the computational domain's lateral boundaries to avoid a discontinuity in ground elevation and in-line-arranged artificial buildings are added to prevent abrupt dissipation of turbulence above the smoothed ground. The size of the (total) computational domain is 7680 m in the x (east–west or streamwise) direction, 2400 m in the y (south–north or spanwise) direction, and 1020 m in the z (vertical) direction. Rectangular grids are used, and the grid size in the x and y directions is 5 m. The grid size in the vertical direction is uniform with 5 m up to $z = 250\text{ m}$ and then increases with an expansion ratio of 1.08 up to z of $\sim 325\text{ m}$, above which it is 10 m. For velocity components and SGS TKE, the radiation boundary condition is applied at the east (outflow) boundary and the cyclic boundary condition is applied at the south and north boundaries. The Dirichlet boundary condition is applied at the top boundary. At the grid points closest to all solid surfaces, Monin–Obukhov similarity is employed in the momentum equation. The roughness length for momentum is set to 0.1 m.

To apply realistic boundary conditions (representing mesoscale wind) in the streamwise direction, the turbulence recycling method (Lund et al. 1998; Kataoka and Mizuno 2002; Park et al. 2015) is employed to generate turbulent inflow data for the main domain. A subdomain in which turbulence is recycled is added in the upstream (west) region of the main domain (see Fig. 2). In the recycling domain, turbulent signals

(perturbations from the horizontal average over the recycling domain) at the outflow boundary ($x = 960$ m) are repeatedly imposed at the inflow boundary ($x = 0$ m). The velocity components at the inflow boundary are expressed as

$$u(x=0 \text{ m}, y, z) = u_{\text{WRF}}(z) + u''(x=960 \text{ m}, y, z),$$

$$v(x=0 \text{ m}, y, z) = v_{\text{WRF}}(z) + v''(x=960 \text{ m}, y, z), \text{ and}$$

$$w(x=0 \text{ m}, y, z) = w''(x=960 \text{ m}, y, z).$$

Here, double prime indicates perturbations from the horizontal average over the recycling domain. WRF-simulated velocity components at four grid points near $(x, y) = (0 \text{ m}, 1200 \text{ m})$ are horizontally averaged and vertically spline interpolated to obtain velocity components u_{WRF} and v_{WRF} . Then the recycled turbulent signals are added to u_{WRF} and v_{WRF} , and the combined data are used as turbulent inflow data (at the west boundary). PALM is integrated for 6 h starting from 0000 UTC 31 May 2008, and 600-s simulation data in seven time periods (0900–0910, 1000–1010, 1100–1110, 1200–1210, 1300–1310, 1400–1410, and 1450–1500 LST 31 May 2008) are analyzed. To obtain initial perturbations (at time $t = 0900$ LST) and mean vertical profiles in the recycling domain, a 2-h precursor simulation with a flat surface and cyclic boundary conditions at the lateral boundaries is conducted prior to the 6-h simulation.

3. Validation

To validate WRF-simulated results, the simulated synoptic fields are compared with the observed fields. The observed and simulated synoptic fields of sea level pressure and wind in the outermost domain at 0000 UTC 31 May 2008 are shown in Fig. 3. The synoptic weather map (Fig. 3a) shows a high pressure system over the east coast of China, which extends to the Korean Peninsula, and two low pressure systems northwest and northeast of the Korean Peninsula. The locations and intensities of the high and low pressure systems are well simulated. The WRF-simulated surface air temperature and wind in the innermost domain are validated by calculating hit rates. Hit rates of 2-m temperature and those of 10-m wind speed and direction in the WRF Model simulation are calculated using observation data from nine automatic weather stations in Seoul. The positions of the nine automatic weather stations are marked in Fig. 1b. The error ranges applied for temperature, wind speed, and wind direction are $\pm 2^\circ\text{C}$, $\pm 1 \text{ m s}^{-1}$, and $\pm 30^\circ$, respectively (Ries and Schlünzen 2009). The calculated hit

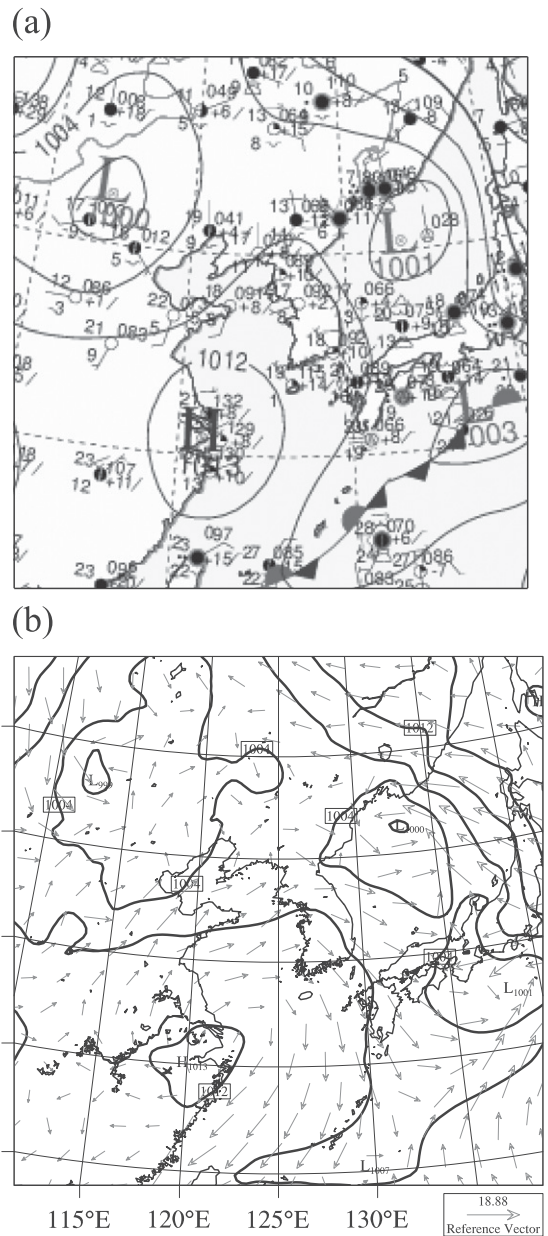


FIG. 3. (a) Observed sea level pressure field (with 4-hPa intervals) and (b) WRF-simulated sea level pressure and wind field in the outermost domain at 0000 UTC 31 May 2008.

rates of temperature, wind speed, and wind direction are 87.1%, 56.4%, and 56.4%, respectively.

Figure 4 shows the time series of observed, WRF-simulated, and PALM-simulated wind speed and wind direction. The observation is made at Gangnam automatic weather station (the station that is indicated with G in Fig. 1b). The WRF-simulated wind speed in the daytime is slightly higher than the observed one, and the change of wind direction around 0900 LST ($\sim 60^\circ$) is not

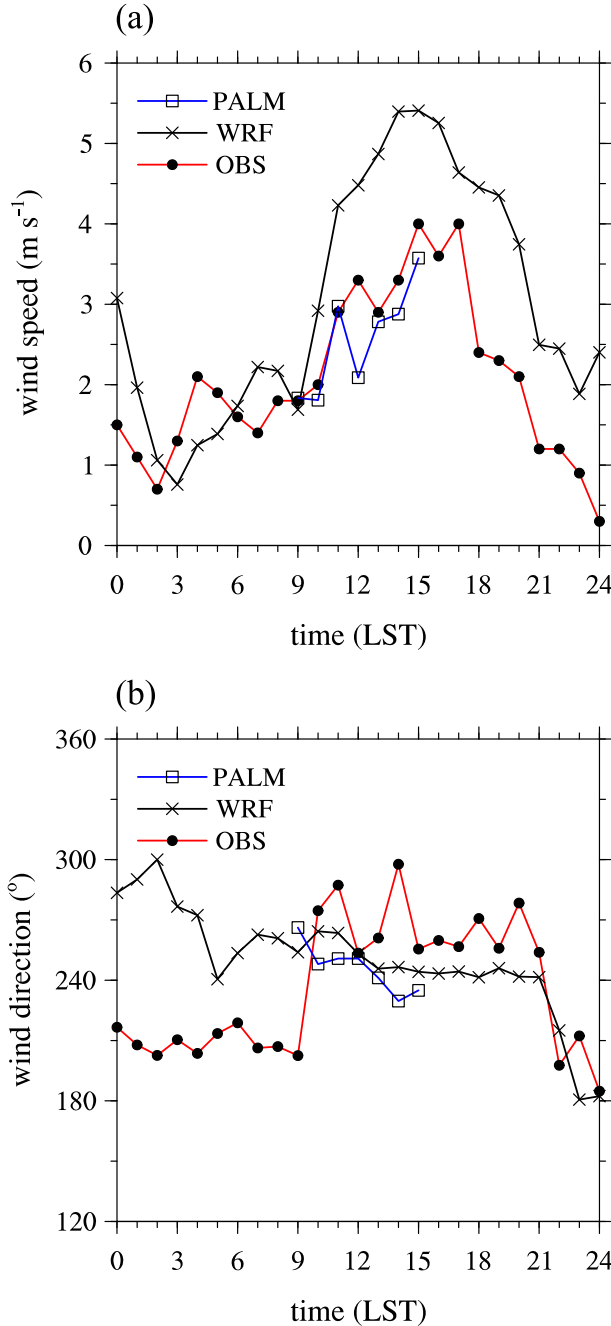


FIG. 4. Temporal variations of observed, WRF-simulated, and PALM-simulated (a) wind speed and (b) wind direction near the surface on 31 May 2008. The observations were made at Gangnam automatic weather station, and the simulation data are interpolated from data at four grid points near the automatic weather station.

simulated in the WRF Model. Despite these discrepancies, the diurnal cycle of wind speed is well simulated. The change of wind direction around 0900 LST is also absent in the time series of PALM-simulated wind

direction. Nevertheless, the observed and PALM-simulated wind speed and direction for the 6-h period are well matched to each other.

4. Results and discussion

a. Turbulent flow

Figure 5 shows the vertical profiles of mean (time averaged) streamwise velocity \bar{u} , mean spanwise velocity \bar{v} , and vertical turbulent momentum flux $\overline{u'w'}$ horizontally averaged over the main domain for 0900–0910, 1100–1110, 1300–1310, and 1450–1500 LST 31 May 2008. As the planetary boundary layer (PBL) develops during the 6-h simulation period, the mean streamwise velocity increases. The vertical variations of mean streamwise velocity and spanwise velocity tend to decrease with height and time above z of ~ 350 m. The PBL mixing, represented by the decreasing vertical variation of mean streamwise velocity and spanwise velocity, results in a nearly constant wind direction ($\sim 250^\circ$) above z of ~ 100 m after 1300 LST. It is noticeable that the magnitude of vertical turbulent momentum flux for 0900–0910 LST increases with height (Fig. 5c). This result indicates that turbulence induced by mesoscale wind (above the surface layer) can be stronger than turbulence induced by buildings above z of ~ 200 m. As time goes on, the vertically increasing trend of vertical turbulent momentum flux disappears and building-induced turbulence dominates. The maximum of vertical turbulent momentum flux magnitude appears at z of ~ 135 m, and the magnitude gradually increases with time.

To illustrate the temporal change of turbulence, the fields of joint probability density function (PDF) of u' and w' for 0900–0910 and 1450–1500 LST and the fields of $u'w'$ multiplied by the joint PDF of u' and w' for 0900–0910 and 1450–1500 LST are plotted in Fig. 6. Here, u' and w' denote deviations from \bar{u} and \bar{w} , and the data at $z = 200$ m in the main domain are sampled to illustrate turbulent eddies induced both by upper flow and by buildings. The joint PDF is calculated using the expression

$$f_{u',w'}(a_i, a_j) = P[a_i - 0.5\Delta a < u' \leq a_i + 0.5\Delta a, a_j - 0.5\Delta a < w' \leq a_j + 0.5\Delta a]$$

(Park et al. 2015). In this expression, a_i (a_j) and Δa are i th (j th) value of variable a and the spacing of bins (0.2), respectively. The number of bins in each direction is 50, and the sum of all joint PDFs is 1. Vertical turbulent momentum flux can be classified into four quadrants: outward interaction ($u'_+ w'_+$), ejection ($u'_- w'_+$), inward

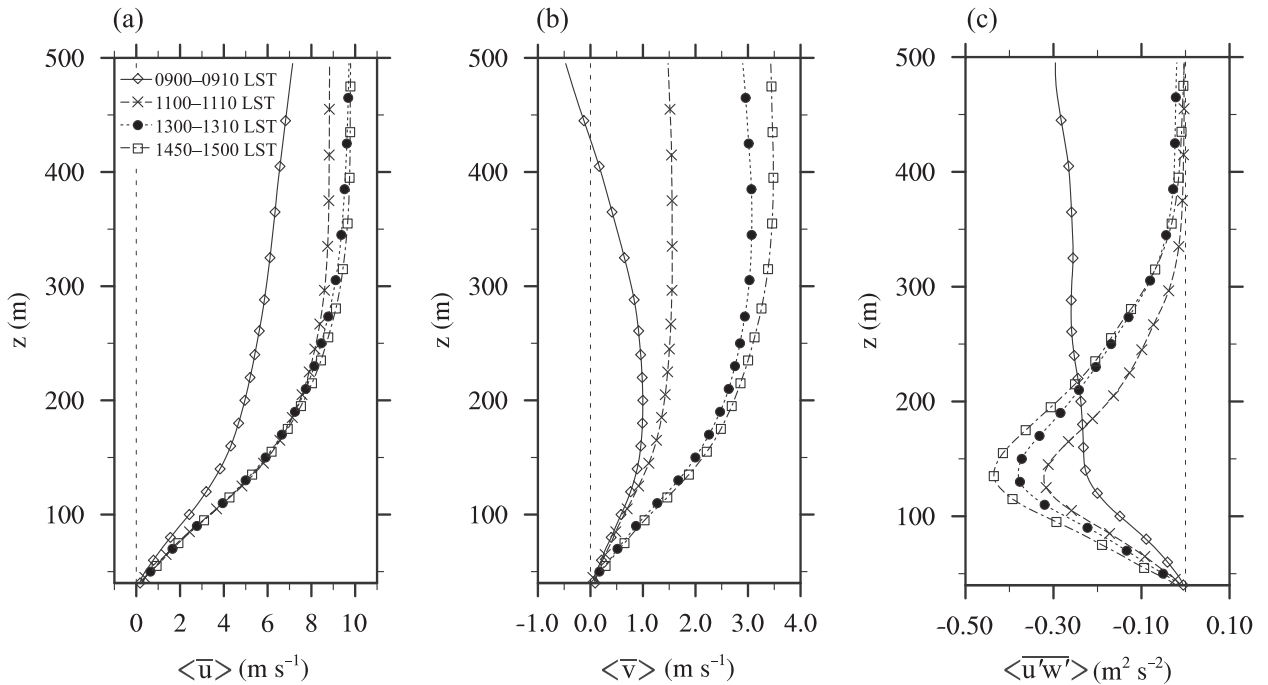


FIG. 5. Vertical profiles of horizontally averaged (a) mean streamwise velocity, (b) mean spanwise velocity, and (c) vertical turbulent momentum flux in the main domain for 0900–0910, 1100–1110, 1300–1310, and 1450–1500 LST 31 May 2008. Overbars and angle brackets indicate time averaging and horizontal averaging, respectively.

interaction ($u'_- w'_-$), and sweep ($u'_+ w'_+$) (Raupach 1981). It appears that the center of the PDF moves from the second quadrant (ejection) to the fourth quadrant (sweep) with time, indicating that sweeps occur more frequently for 1450–1500 LST than for 0900–0910 LST at $z = 200$ m. The fields of $u'w'$ multiplied by the joint PDF also indicate that weak ejections and stronger sweeps play a dominant role in transporting momentum downward for 0900–0910 LST and that strong ejections and weaker sweeps play a dominant role in transporting momentum downward for 1450–1500 LST (Figs. 6c,d).

Figure 7 shows conditionally averaged vertical-velocity-perturbation and velocity-perturbation vector fields for 0900–0910 and 1450–1500 LST. Data around the local minimum points of $u'w'$ in the x - y plane ($z = 200$ m), satisfying a certain criterion (e.g., $u'w' < -2 \text{ m}^2 \text{s}^{-2}$), are sampled and averaged to extract turbulence coherent structures for each period. Sweeps induced by upper flow and ejections are dominant for 0900–0910 and 1450–1500 LST, respectively. The coherent structure for 0900–0910 LST is tilted to the south (Fig. 7b), and its spatial scale is very large. Conversely, the coherent structure for 1450–1500 LST does not show any directional tendency in the spanwise direction, and its spatial scale is smaller than 100 m. The coherent structure for 1450–1500 LST seems to be induced by buildings or building-induced flow structures in the surface layer.

To investigate the relationship between canopy-layer flow and mesoscale wind, data at $z' = 2.5$ m (here, z' indicates the height above streets and the height is mostly close to pedestrian level) are extracted and analyzed. Figure 8 shows the time series of mean (600-s averaged) reference wind speed V_{ref} at $z = 600$ m (representing mesoscale wind) and mean wind speed $\langle V_p \rangle$, mean streamwise velocity $\langle \bar{u}_p \rangle$, and $\langle \text{TKE}_p \rangle$ at 2.5 m above street surfaces. Here, angle brackets indicate horizontal averaging. The urban area is divided into the area occupied by buildings and the area without buildings (mostly streets), and quantities at 2.5 m above the bottom surface in the area without buildings are calculated. The reference mean wind speed increases with time, and the mean wind speed at pedestrian level also increases. The pedestrian mean wind speed increases more slowly after 1100 LST than before 1100 LST, however. This might be related to changes in flow intensity in the building canopy layer after 1100 LST. The pedestrian mean streamwise velocity tends to decrease after 1100 LST, and this decrease can again be attributed to changes in flow intensity. As mesoscale wind strengthens with enhanced PBL mixing, vortices become strong in the south–north-aligned streets (nearly perpendicular to the mean flow direction). The pedestrian TKE increases after 1000 LST, and the reference mean wind speed evinces a similar increase at $z = 600$ m.

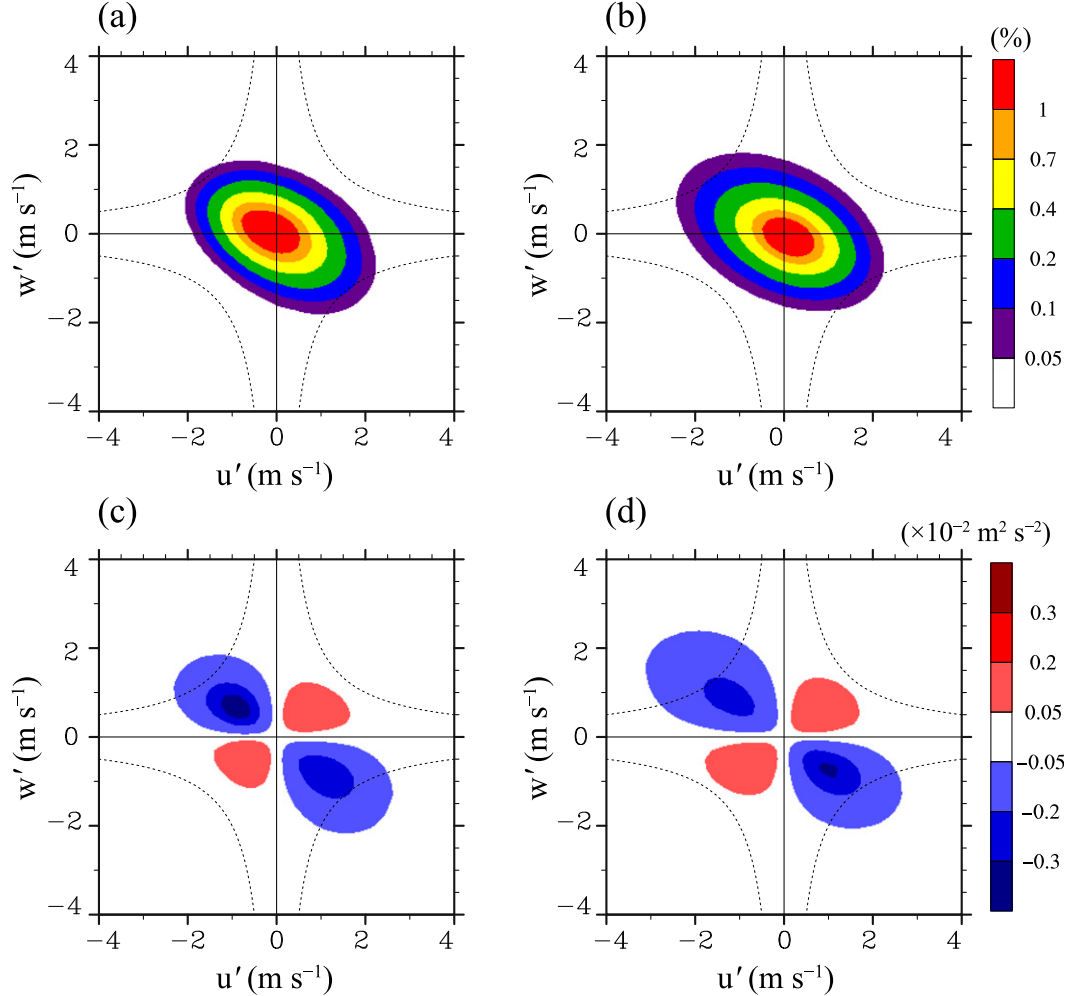


FIG. 6. Fields of the joint probability density function of u' and w' at $z = 200$ m in the main domain for (a) 0900–0910 and (b) 1450–1500 LST and $u'w'$ multiplied by the joint probability density function of u' and w' at $z = 200$ m in the main domain for (c) 0900–0910 and (d) 1450–1500 LST. Dashed lines of equal $|u'w'|$ ($2 \text{ m}^2 \text{ s}^{-2}$) are added.

Figure 9 shows the multiresolution spectra of streamwise velocity, spanwise velocity, and vertical velocity at $(x, y, z') = (5132.5, 2082.5, 2.5 \text{ m})$, $(4172.5, 1022.5, 2.5 \text{ m})$, and $(3502.5, 1987.5, 2.5 \text{ m})$. The spectra are normalized by their maximum values, and the three points are located in a street canyon, an intersection, and a dense building area, respectively. To investigate nonperiodic variations at $z' = 2.5 \text{ m}$ in the entire main domain, the multiresolution spectrum analysis using the fast Haar transform algorithm is conducted (Howell and Mahrt 1997; Vickers and Mahrt 2003). The spectra of streamwise and spanwise velocities have their maximum values at 80- or 160-s time scale, and those of vertical velocity have their maximum values at 80-s time scale in the dense building area and 10-s time scale in the street canyon and intersection. Although the spectra of vertical velocity have maximum values at smaller time scale than those of

horizontal velocities in the street canyon and intersection [as in the urban surface layer in Roth (2000)], the shape of spectra in the dense building area seems to be independent of which velocity component is plotted. It is also remarkable that the multiresolution spectra in the dense building area at large time scales (≥ 2560 s) tend to decrease monotonically with increasing time scale, indicating strong decoupling from mesoscale wind. In contrast to the variations in the dense building area, variations with 10240-s (~ 2.8 h) or 20480-s (~ 5.7 h) time scale are distinct in the spectra of streamwise velocity in the street canyon and intersection. While the spectrum of spanwise velocity in the intersection also has distinct variations at time scales larger than or equal to 10240 s, that in the street canyon does not have distinct variations at the time scales (≥ 10240 s) because of the formation of canyon vortices (Fig. 12a). Despite a large spatial

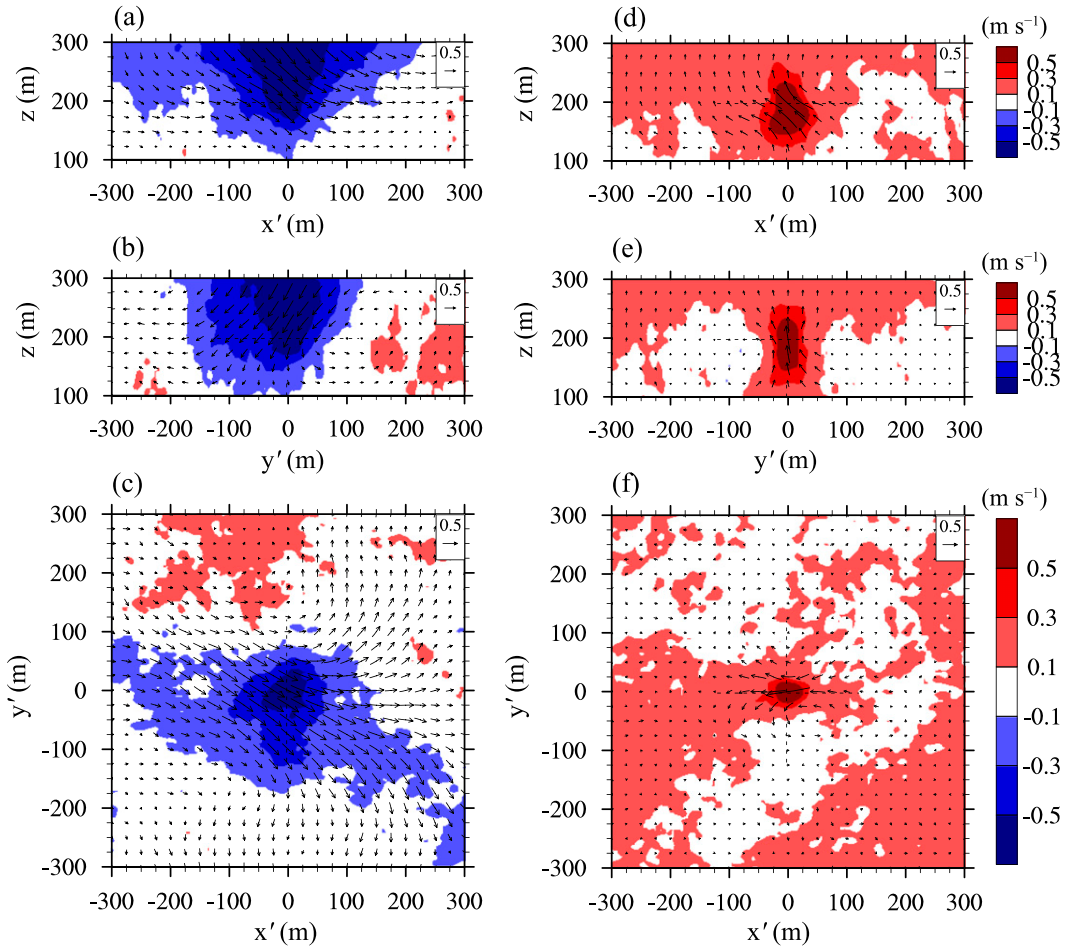


FIG. 7. Conditionally averaged w' (color shading) and velocity-perturbation vector (u' , v' , and w') fields for 0900–0910 LST in the (a) x' - z plane ($y' = 0$ m), (b) y' - z plane ($x' = 0$ m), and (c) x' - y' plane ($z = 200$ m). (d),(e),(f) As in (a), (b), and (c), but for 1450–1500 LST.

variability of multiresolution spectra in the main domain (not shown), the variations at large time scales indicate that mesoscale wind definitely affects turbulent flow close to the pedestrian level.

To further investigate the turbulent flow close to the pedestrian level, the PDFs of normalized streamwise-velocity increments and normalized vertical-velocity increments for 0900–1500 LST at $(x, y, z') = (5132.5, 2082.5, 2.5\text{ m})$, $(4172.5, 1022.5, 2.5\text{ m})$, and $(3502.5, 1987.5, 2.5\text{ m})$ are plotted in Fig. 10. The streamwise-velocity and vertical-velocity increments are calculated using the expressions $u_\tau(t) = u(t + \tau) - u(t)$ and $w_\tau(t) = w(t + \tau) - w(t)$, respectively, where τ is a time lag (Böttcher et al. 2007). The PDFs with 5-s, 1-min, and 10-min time lags are shown with red Gaussian distribution curves in Fig. 10, and the PDFs with 1-min and 10-min time lags are divided by 30 and 900, respectively, to show each PDF clearly without overlays. The distribution of streamwise-velocity increments changes from

“stretched” exponential to nearly Gaussian with an increasing time lag, as shown in previous studies (Böttcher et al. 2007; Muzy et al. 2010). A similar trend appears in the PDFs of vertical-velocity increments (Fig. 10b). The PDFs of streamwise, vertical, and spanwise (not shown) velocities become nearly Gaussian even at the 1-min time lag, whereas the PDF of surface-layer wind in Muzy et al. (2010) has large tails at a 1-h time lag. This difference could be attributed to more intermittent cascade by nonstationary background wind or building-induced flow in the building canopy layer than in the surface layer in Muzy et al. (2010), but there is no distinct spatial difference between the PDFs as compared with the significant spatial difference in the multiresolution spectra of velocity components. The PDFs from different sampling periods (e.g., 0900–1100 and 1300–1500 LST) are compared with each other but the differences are not noticeable. Further study, focusing on time-varying turbulence statistics, is required to further understand

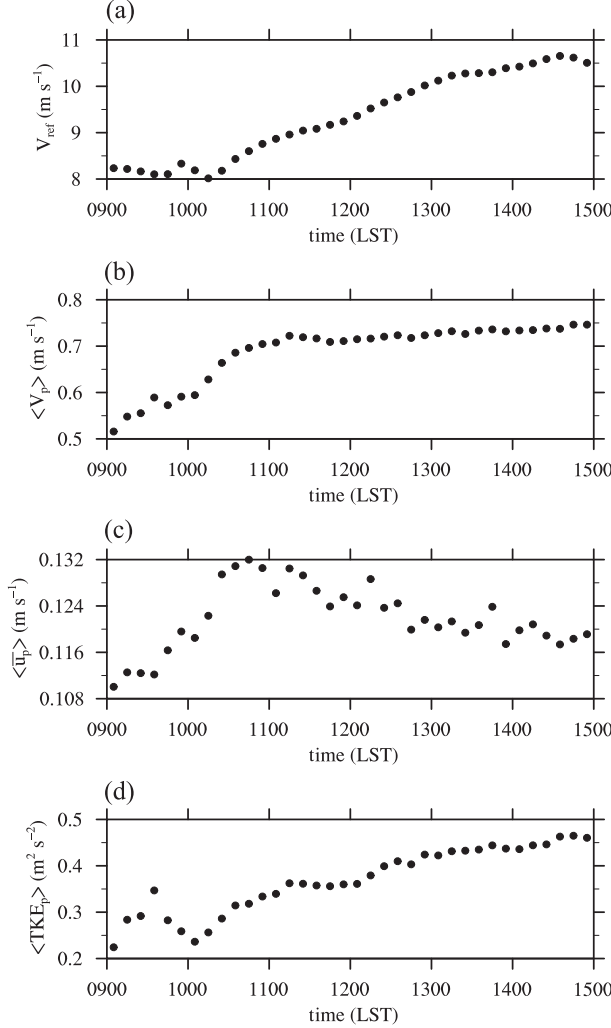


FIG. 8. Temporal variations of (a) reference wind speed at $z = 600$ m and horizontally averaged (b) mean wind speed, (c) mean streamwise velocity, and (d) TKE at $z' = 2.5$ m in the main domain.

the impacts of mesoscale wind on urban-scale turbulent flow.

b. Ventilation

To investigate ventilation in the densely built-up urban area, the ratios of mean wind speed at pedestrian level to the reference mean wind speed (Letzel et al. 2012) at $z = 600$ m for 0900–0910 and 1450–1500 LST are calculated and plotted in Fig. 11. The velocity ratio is high on broad streets and at intersections. The velocity ratio is also high around an apartment complex at $(x, y) \approx (3120, 1200)$ m, but the high ratio might be due to the absence of upstream tall buildings. In contrast to the high velocity ratio on broad streets, velocity ratios in dense building areas are low because of the blockage of pedestrian wind. Differences between the velocity ratio

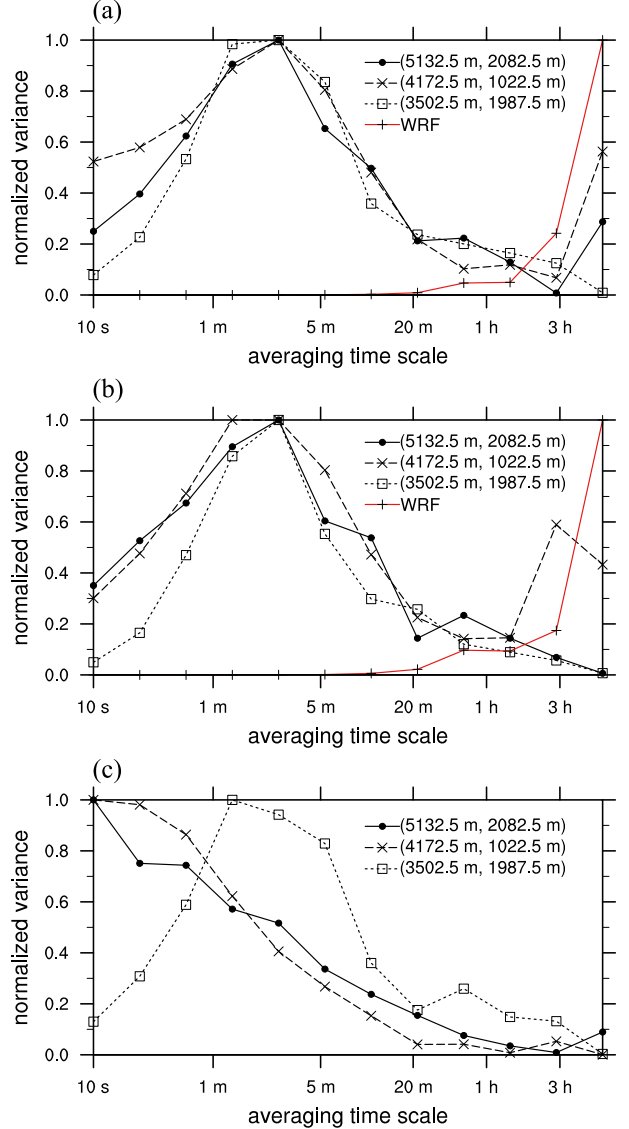


FIG. 9. Multiresolution spectra of (a) streamwise velocity, (b) spanwise velocity, and (c) vertical velocity at $z' = 2.5$ m over the three points that are described in the text. The multiresolution spectra of WRF-simulated streamwise and spanwise velocities at $z = 600$ m are added in (a) and (b), respectively.

fields during the two periods are small except in magnitude, however.

Figure 12 shows the fields of vertical velocity and streamline in the x - y plane ($z = 60$ m) and in the x - z plane ($y = 1860$ m) for 0900–0910 LST. Because of the formation of vortices in streets, the pedestrian mean wind speed increases. Around intersections, downward and upward flows appear near the wake region of upstream buildings. For example, the tall building at $(x, y) \approx (4140, 960)$ m induces downward winding flow around it at $z = 60$ m, and upward flow appears in the intersection

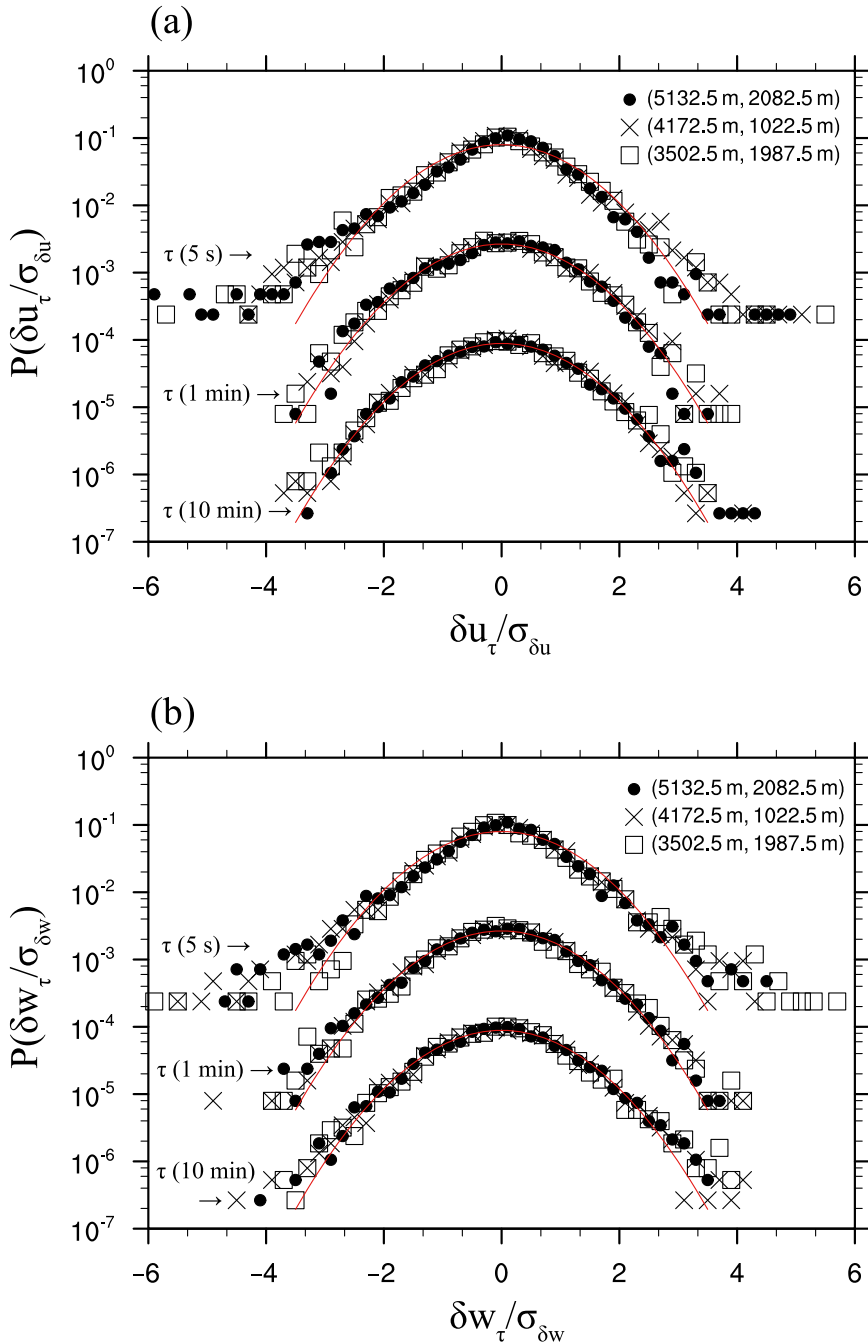


FIG. 10. PDFs of (a) normalized streamwise-velocity increments and (b) normalized vertical-velocity increments at $z' = 2.5$ m over the three points. The PDFs with 1- and 10-min time lags are divided by 30 and 900, respectively, to avoid overlaps. Red lines represent Gaussian distribution curves.

$(x, y) \approx (4170, 1020)$ m. The magnitude of vertical velocity becomes large because of the existence of tall buildings around the intersection, and the updrafts and downdrafts seem to actively transport momentum downward, resulting in active ventilation.

Figure 13 shows the scatterplot of $\langle V_p \rangle / V_{\text{ref}}$ and V_{ref} and that of $\langle V_p \rangle / V_{\text{ref}}$ and $\langle \bar{u}_p \rangle$. The velocity ratio $\langle V_p \rangle / V_{\text{ref}}$ decreases with increasing mesoscale wind after 1020 LST. This can be attributed to mesoscale wind speed, which increases more rapidly than pedestrian

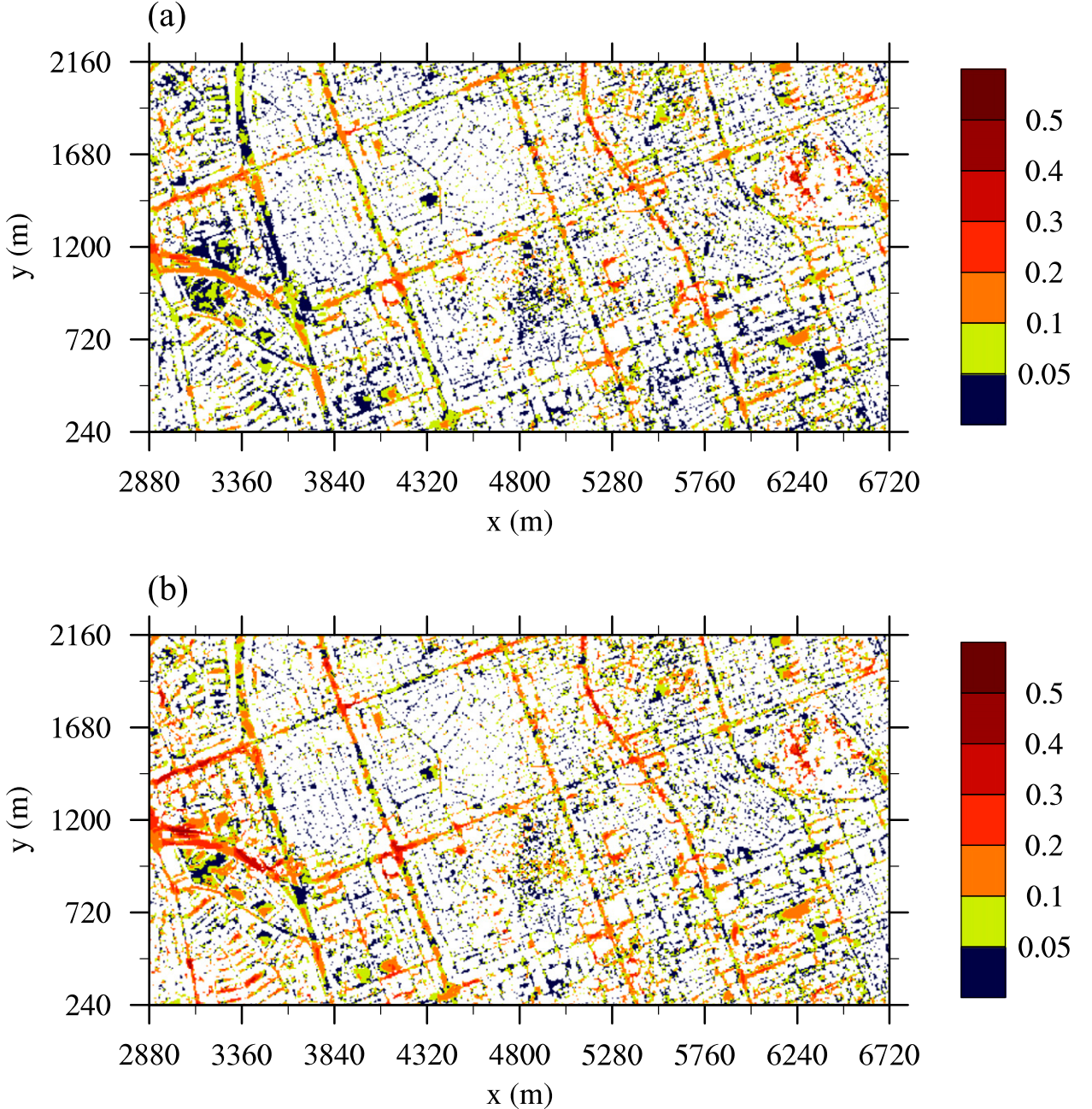


FIG. 11. Fields of time-averaged velocity ratio V_p/V_{ref} in the main domain for (a) 0900–0910 and (b) 1450–1500 LST.

mean wind speed. Thus, the velocity ratio can be sensitive to the reference level and cannot perfectly represent ventilation in the case in which the reference wind speed itself changes. This indicates that the dependency of velocity ratio on mesoscale wind is complex. In contrast to the pedestrian mean wind speed, the pedestrian mean streamwise velocity is linearly proportional to the velocity ratio, indicating the possibility of pedestrian mean streamwise velocity being used as a ventilation

indicator. This indicator should, however, first undergo additional testing for more cases.

5. Summary and conclusions

Turbulent flow in a densely built-up area of Seoul for 0900–1500 LST 31 May 2008 was simulated using an LES model coupled to a mesoscale model (WRF). The time-varying inflow condition (the sum of mesoscale

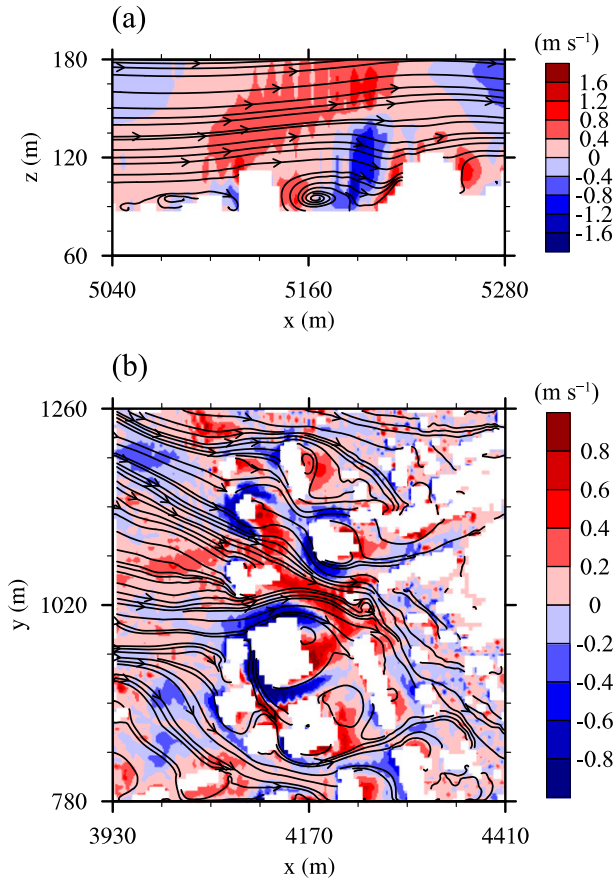


FIG. 12. Fields of mean vertical velocity (color shading) and streamline in the (a) x - z plane ($y = 1860$ m) and (b) x - y plane ($z = 60$ m) for 0900–0910 LST.

wind and recycled turbulent signals) induces very different turbulence structures depending on time. Weak ejections and stronger sweeps are dominant for 0900–0910 LST, whereas strong ejections and weaker sweeps are dominant for 1450–1500 LST at $z = 200$ m, and the strong ejections seem to be induced by buildings or by building-induced flow structures. The pedestrian (2.5 m above street surfaces) mean wind speed and pedestrian TKE increase during the simulation period while the pedestrian mean streamwise velocity decreases after 1100 LST. The multiresolution spectra of velocity components illustrate their temporal variations related to mesoscale wind, especially in a street canyon and an intersection. The variations induced by mesoscale wind disappear in a dense building area, however, indicating strong decoupling from mesoscale wind. In contrast to the multiresolution spectra, the probability density distributions of normalized streamwise-velocity and vertical-velocity increments do not show any noticeable spatial variability. Instead, they change from “stretched” exponential to nearly Gaussian with an increasing time lag,

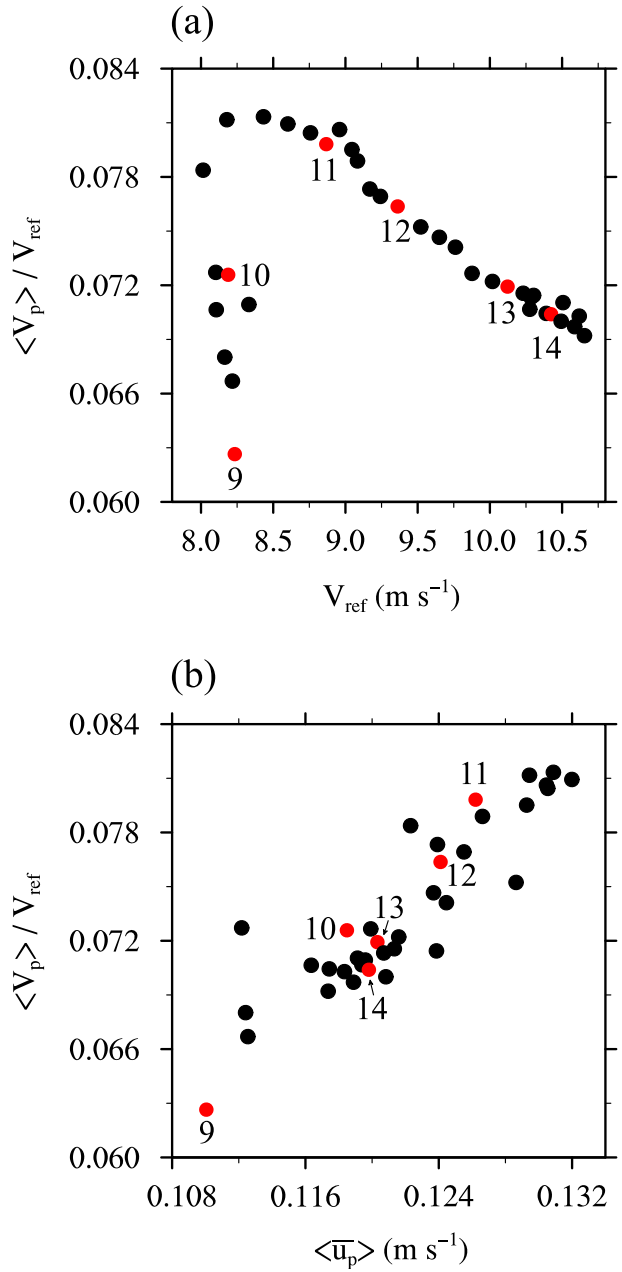


FIG. 13. Scatterplots of (a) velocity ratio and reference mean wind speed and (b) velocity ratio and horizontally averaged pedestrian mean streamwise velocity. Each point shows 600-s averaged quantities, and results for every six periods are indicated by red dots and starting local time.

illustrating a universal distribution trend. The velocity ratio of the pedestrian mean wind speed to the reference mean wind speed (at $z = 600$ m) indicates ventilation in the urban area, and it is high on broad streets and at intersections and low in dense building areas.

In this study, the ratio of the pedestrian wind speed to the reference wind speed is used to indicate ventilation

in the urban area, but the velocity ratio is sensitive to the reference level and selecting the reference level in a developing atmospheric boundary layer is very difficult and needs further investigation. One possible alternative to the velocity ratio is an indicator that is based on pollutant-dispersion rates. To explore this possibility, further study is required to investigate pollutant dispersion in densely built-up urban areas using a building-resolving CFD model coupled to a mesoscale model.

Acknowledgments. The authors are grateful to three anonymous reviewers for providing valuable comments on this work. This work was supported by National Research Foundation of Korea (NRF) Grant 2011-0017041 funded by the Korea Ministry of Science, ICT and Future Planning (MSIP).

REFERENCES

- Baik, J.-J., and J.-J. Kim, 1999: A numerical study of flow and pollutant dispersion characteristics in urban street canyons. *J. Appl. Meteor.*, **38**, 1576–1589, doi:[10.1175/1520-0450\(1999\)038<1576:ANSOFA>2.0.CO;2](https://doi.org/10.1175/1520-0450(1999)038<1576:ANSOFA>2.0.CO;2).
- , S.-B. Park, and J.-J. Kim, 2009: Urban flow and dispersion simulation using a CFD model coupled to a mesoscale model. *J. Appl. Meteor. Climatol.*, **48**, 1667–1681, doi:[10.1175/2009JAMC2066.1](https://doi.org/10.1175/2009JAMC2066.1).
- Balogun, A. A., and Coauthors, 2010: In-street wind direction variability in the vicinity of a busy intersection in central London. *Bound.-Layer Meteor.*, **136**, 489–513, doi:[10.1007/s10546-010-9515-y](https://doi.org/10.1007/s10546-010-9515-y).
- Böttcher, F., St. Barth, and J. Peinke, 2007: Small and large scale fluctuations in atmospheric wind speeds. *Stochastic Environ. Res. Risk Assess.*, **21**, 299–308, doi:[10.1007/s00477-006-0065-2](https://doi.org/10.1007/s00477-006-0065-2).
- Chen, F., and J. Dudhia, 2001: Coupling an advanced land-surface-hydrology model with the Penn State–NCAR MM5 modeling system. Part I: Model implementation and sensitivity. *Mon. Wea. Rev.*, **129**, 569–585, doi:[10.1175/1520-0493\(2001\)129<0569:CAALSH>2.0.CO;2](https://doi.org/10.1175/1520-0493(2001)129<0569:CAALSH>2.0.CO;2).
- Cheng, H., and I. P. Castro, 2002: Near wall flow over urban-like roughness. *Bound.-Layer Meteor.*, **104**, 229–259, doi:[10.1023/A:1016060103448](https://doi.org/10.1023/A:1016060103448).
- Coceal, O., T. G. Thomas, I. P. Castro, and S. E. Belcher, 2006: Mean flow and turbulence statistics over groups of urban-like cubical obstacles. *Bound.-Layer Meteor.*, **121**, 491–519, doi:[10.1007/s10546-006-9076-2](https://doi.org/10.1007/s10546-006-9076-2).
- Cox, C. F., B. Z. Cybyk, J. P. Boris, Y. T. Fung, and S. W. Chang, 2000: Coupled microscale-mesoscale modeling of contaminant transport in urban environments. Abstracts, *Third Symp. on the Urban Environment*, Davis, CA, Amer. Meteor. Soc., 8.2. [Available online at https://ams.confex.com/ams/AugDavis/techprogram/paper_15208.htm.]
- Deardorff, J. W., 1980: Stratocumulus-capped mixed layers derived from a three-dimensional model. *Bound.-Layer Meteor.*, **18**, 495–527, doi:[10.1007/BF00119502](https://doi.org/10.1007/BF00119502).
- Dudhia, J., 1989: Numerical study of convection observed during the winter monsoon experiment using a mesoscale two-dimensional model. *J. Atmos. Sci.*, **46**, 3077–3107, doi:[10.1175/1520-0469\(1989\)046<3077:NSOCOD>2.0.CO;2](https://doi.org/10.1175/1520-0469(1989)046<3077:NSOCOD>2.0.CO;2).
- Ehrhard, J., I. Khatib, C. Winkler, R. Kunz, N. Moussiopoulos, and G. Ernst, 2000: The microscale model MIMO: Development and assessment. *J. Wind Eng. Ind. Aerodyn.*, **85**, 163–176, doi:[10.1016/S0167-6105\(99\)00137-3](https://doi.org/10.1016/S0167-6105(99)00137-3).
- Eliasson, I., B. Offerle, C. S. B. Grimmond, and S. Lindqvist, 2006: Wind fields and turbulence statistics in an urban street canyon. *Atmos. Environ.*, **40**, 1–16, doi:[10.1016/j.atmosenv.2005.03.031](https://doi.org/10.1016/j.atmosenv.2005.03.031).
- Hong, S.-Y., and J.-O. J. Lim, 2006: The WRF single-moment 6-class microphysics scheme (WSM6). *J. Korean Meteor. Soc.*, **42**, 129–151.
- , Y. Noh, and J. Dudhia, 2006: A new vertical diffusion package with an explicit treatment of entrainment processes. *Mon. Wea. Rev.*, **134**, 2318–2341, doi:[10.1175/MWR3199.1](https://doi.org/10.1175/MWR3199.1).
- Howell, J. F., and L. Mahrt, 1997: Multiresolution flux decomposition. *Bound.-Layer Meteor.*, **83**, 117–137, doi:[10.1023/A:1000210427798](https://doi.org/10.1023/A:1000210427798).
- Inagaki, A., and M. Kanda, 2010: Organized structure of active turbulence over an array of cubes within the logarithmic layer of atmospheric flow. *Bound.-Layer Meteor.*, **135**, 209–228, doi:[10.1007/s10546-010-9477-0](https://doi.org/10.1007/s10546-010-9477-0).
- Kain, J. S., 2004: The Kain–Fritsch convective parameterization: An update. *J. Appl. Meteor.*, **43**, 170–181, doi:[10.1175/1520-0450\(2004\)043<0170:TKCPAU>2.0.CO;2](https://doi.org/10.1175/1520-0450(2004)043<0170:TKCPAU>2.0.CO;2).
- Kanda, M., A. Inagaki, T. Miyamoto, M. Gryschka, and S. Raasch, 2013: A new aerodynamic parametrization for real urban surfaces. *Bound.-Layer Meteor.*, **148**, 357–377, doi:[10.1007/s10546-013-9818-x](https://doi.org/10.1007/s10546-013-9818-x).
- Kataoka, H., and M. Mizuno, 2002: Numerical flow computation around aeroelastic 3D square cylinder using inflow turbulence. *Wind Struct.*, **5**, 379–392, doi:[10.12989/was.2002.5.2_3_4.379](https://doi.org/10.12989/was.2002.5.2_3_4.379).
- Kim, J.-J., and J.-J. Baik, 2004: A numerical study of the effects of ambient wind direction on flow and dispersion in urban street canyons using the RNG $k-e$ turbulence model. *Atmos. Environ.*, **38**, 3039–3048, doi:[10.1016/j.atmosenv.2004.02.047](https://doi.org/10.1016/j.atmosenv.2004.02.047).
- Letzel, M. O., M. Krane, and S. Raasch, 2008: High resolution urban large-eddy simulation studies from street canyon to neighbourhood scale. *Atmos. Environ.*, **42**, 8770–8784, doi:[10.1016/j.atmosenv.2008.08.001](https://doi.org/10.1016/j.atmosenv.2008.08.001).
- , C. Helmke, E. Ng, X. An, A. Lai, and S. Raasch, 2012: LES case study on pedestrian level ventilation in two neighbourhoods in Hong Kong. *Meteor. Z.*, **21**, 575–589, doi:[10.1127/0941-2948/2012/0356](https://doi.org/10.1127/0941-2948/2012/0356).
- Li, X., C. Liu, D. Leung, and K. Lam, 2006: Recent progress in CFD modelling of wind field and pollutant transport in street canyons. *Atmos. Environ.*, **40**, 5640–5658, doi:[10.1016/j.atmosenv.2006.04.055](https://doi.org/10.1016/j.atmosenv.2006.04.055).
- Liu, Y. S., S. G. Miao, C. L. Zhang, G. X. Cui, and Z. S. Zhang, 2012: Study on micro-atmospheric environment by coupling large eddy simulation with mesoscale model. *J. Wind Eng. Ind. Aerodyn.*, **107–108**, 106–117, doi:[10.1016/j.jweia.2012.03.033](https://doi.org/10.1016/j.jweia.2012.03.033).
- Lund, T. S., X. Wu, and K. D. Squires, 1998: Generation of turbulent inflow data for spatially-developing boundary layer simulations. *J. Comput. Phys.*, **140**, 233–258, doi:[10.1006/jcph.1998.5882](https://doi.org/10.1006/jcph.1998.5882).
- Mlawer, E. J., S. J. Taubman, P. D. Brown, M. J. Iacono, and S. A. Clough, 1997: Radiative transfer for inhomogeneous atmospheres: RRTM, a validated correlated- k model for the longwave. *J. Geophys. Res.*, **102**, 16 663–16 682, doi:[10.1029/97JD00237](https://doi.org/10.1029/97JD00237).
- Muzy, J.-F., R. Baile, and P. Poggi, 2010: Intermittency of surface-layer wind velocity series in the mesoscale range. *Phys. Rev.*, **81E**, 056308, doi:[10.1103/PhysRevE.81.056308](https://doi.org/10.1103/PhysRevE.81.056308).
- Nakayama, H., T. Takemi, and H. Nagai, 2011: LES analysis of the aerodynamic surface properties for turbulent flows over

- building arrays with various geometries. *J. Appl. Meteor. Climatol.*, **50**, 1692–1712, doi:[10.1175/2011JAMC2567.1](https://doi.org/10.1175/2011JAMC2567.1).
- , —, and —, 2012: Large-eddy simulation of urban boundary-layer flows by generating turbulent inflows from mesoscale meteorological simulations. *Atmos. Sci. Lett.*, **13**, 180–186, doi:[10.1002/asl.377](https://doi.org/10.1002/asl.377).
- Park, S.-B., J.-J. Baik, and B.-S. Han, 2015: Large-eddy simulation of turbulent flow in a densely built-up urban area. *Environ. Fluid Mech.*, **15**, 235–250, doi:[10.1007/s10652-013-9306-3](https://doi.org/10.1007/s10652-013-9306-3).
- Piacsek, S. A., and G. P. Williams, 1970: Conservation properties of convection difference schemes. *J. Comput. Phys.*, **6**, 392–405, doi:[10.1016/0021-9991\(70\)90038-0](https://doi.org/10.1016/0021-9991(70)90038-0).
- Princevac, M., J.-J. Baik, X. Li, H. Pan, and S.-B. Park, 2010: Lateral channelling within rectangular arrays of cubical obstacles. *J. Wind Eng. Ind. Aerodyn.*, **98**, 377–385, doi:[10.1016/j.jweia.2009.11.001](https://doi.org/10.1016/j.jweia.2009.11.001).
- Raasch, S., and M. Schröter, 2001: PALM—A large-eddy simulation model performing on massively parallel computers. *Meteor. Z.*, **10**, 363–372, doi:[10.1127/0941-2948/2001/0010-0363](https://doi.org/10.1127/0941-2948/2001/0010-0363).
- Raupach, M. R., 1981: Conditional statistics of Reynolds stress in rough-wall and smooth-wall turbulent boundary layers. *J. Fluid Mech.*, **108**, 363–382, doi:[10.1017/S0022112081002164](https://doi.org/10.1017/S0022112081002164).
- Ries, H., and K. H. Schlünzen, 2009: Evaluation of a mesoscale model with different surface parameterizations and vertical resolutions for the bay of Valencia. *Mon. Wea. Rev.*, **137**, 2646–2661, doi:[10.1175/2009MWR2836.1](https://doi.org/10.1175/2009MWR2836.1).
- Roth, M., 2000: Review of atmospheric turbulence over cities. *Quart. J. Roy. Meteor. Soc.*, **126**, 941–990, doi:[10.1002/qj.49712656409](https://doi.org/10.1002/qj.49712656409).
- Ryu, Y.-H., J.-J. Baik, and S.-H. Lee, 2011: A new single-layer urban canopy model for use in mesoscale atmospheric models. *J. Appl. Meteor. Climatol.*, **50**, 1773–1794, doi:[10.1175/2011JAMC2665.1](https://doi.org/10.1175/2011JAMC2665.1).
- Santos, J. M., N. C. Reis Jr., E. V. Goulart, and I. Mavroidis, 2009: Numerical simulation of flow and dispersion around an isolated cubical building: The effect of the atmospheric stratification. *Atmos. Environ.*, **43**, 5484–5492, doi:[10.1016/j.atmosenv.2009.07.020](https://doi.org/10.1016/j.atmosenv.2009.07.020).
- Skamarock, W. C., and Coauthors, 2008: A description of the Advanced Research WRF version 3. NCAR Tech. Note NCAR/TN-475+STR, 113 pp. [Available online at http://www.mmm.ucar.edu/wrf/users/docs/arw_v3_bw.pdf.]
- Vickers, D., and L. Mahrt, 2003: The cospectral gap and turbulent flux calculations. *J. Atmos. Oceanic Technol.*, **20**, 660–672, doi:[10.1175/1520-0426\(2003\)20<660:TCGATF>2.0.CO;2](https://doi.org/10.1175/1520-0426(2003)20<660:TCGATF>2.0.CO;2).
- Wyszogrodzki, A. A., S. Miao, and F. Chen, 2012: Evaluation of the coupling between mesoscale-WRF and LES-EULAG models for simulating fine-scale urban dispersion. *Atmos. Res.*, **118**, 324–345, doi:[10.1016/j.atmosres.2012.07.023](https://doi.org/10.1016/j.atmosres.2012.07.023).
- Xie, Z.-T., 2011: Modelling street-scale flow and dispersion in realistic winds—Towards coupling with mesoscale meteorological models. *Bound.-Layer Meteor.*, **141**, 53–75, doi:[10.1007/s10546-011-9629-x](https://doi.org/10.1007/s10546-011-9629-x).
- Zhang, Y. Q., S. P. Arya, and W. H. Snyder, 1996: A comparison of numerical and physical modeling of stable atmospheric flow and dispersion around a cubical building. *Atmos. Environ.*, **30**, 1327–1345, doi:[10.1016/1352-2310\(95\)00326-6](https://doi.org/10.1016/1352-2310(95)00326-6).